

Improving Photocatalytic Water Treatment through Nanocrystal Engineering: Mesoporous Nanosheet-Assembled 3D BiOCl Hierarchical Nanostructures That Induce Unprecedented Large Vacancies

Sheng-qi Guo,^{†,‡} Xiao-he Zhu,[†] Hai-jun Zhang,[§] Bing-chuan Gu,^{||} Wei Chen,^{*,†} Lu Liu,^{*,†} and Pedro J. J. Alvarez^{*,†}

[†]Tianjin Key Laboratory of Environmental Remediation and Pollution Control, College of Environmental Science and Engineering, Nankai University, Tianjin 300350, China

[‡]Tianjin Key Lab for Photoelectric Materials & Devices, School of Materials Science and Engineering, Tianjin University of Technology, Tianjin 300384, China

[§]School of Physics and Materials Science, Anhui University, Hefei, Anhui 230039, China

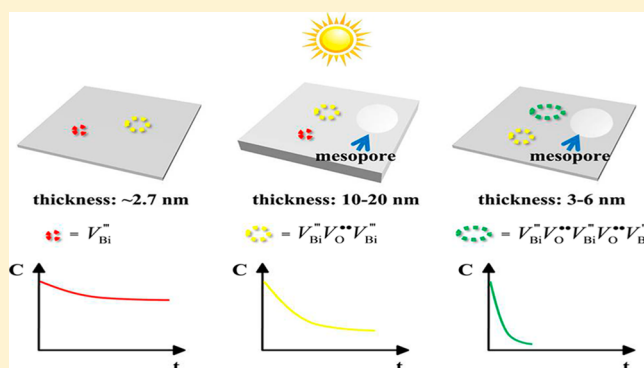
^{||}State Key Laboratory of Particle Detection and Electronics, University of Science & Technology of China, Hefei, Anhui 230026, China

[⊥]Department of Civil and Environmental Engineering, Rice University, Houston, Texas 77005, United States

Supporting Information

ABSTRACT: Vacancy control can significantly enhance the performance of photocatalytic semiconductors for water purification. However, little is known about the mechanisms and approaches that could generate stable large vacancies. Here, we report a new mechanism to induce vacancy formation on nanocrystals for enhanced photocatalytic activity: the introduction of mesopores. We synthesized two nanosheet-assembled hierarchical 3D BiOCl mesoporous nanostructures with similar morphology and exposed facets but different nanosheet thickness. Positron annihilation analysis detected unprecedentedly large $V_{\text{Bi}}^{\text{III}}V_{\text{O}}^{\text{II}}V_{\text{Bi}}^{\text{III}}V_{\text{O}}^{\text{II}}V_{\text{Bi}}^{\text{III}}$ vacancy associates (as well as $V_{\text{Bi}}^{\text{III}}V_{\text{O}}^{\text{II}}V_{\text{Bi}}^{\text{III}}$) on BiOCl assembled from 3–6 nm nanosheets but only $V_{\text{Bi}}^{\text{III}}V_{\text{O}}^{\text{II}}V_{\text{Bi}}^{\text{III}}$ vacancy associates on BiOCl assembled from thicker (10–20 nm) nanosheets.

Comparison of vacancy properties with 2D ultrathin 2.7 nm nanosheets (with $V_{\text{Bi}}^{\text{III}}V_{\text{O}}^{\text{II}}V_{\text{Bi}}^{\text{III}}$ and $V_{\text{Bi}}^{\text{III}}$) indicates that nanosheet thinness alone cannot explain the formation of such large atom vacancies. On the basis of density functional theory computations of formation energy of isolated Bi vacancy, we show that mesopores facilitate the formation of large vacancies to counterbalance thermodynamic instability caused by incompletely coordinated Bi and O atoms along the mesopore perimeters. We corroborate that the extraordinarily large $V_{\text{Bi}}^{\text{III}}V_{\text{O}}^{\text{II}}V_{\text{Bi}}^{\text{III}}V_{\text{O}}^{\text{II}}V_{\text{Bi}}^{\text{III}}$ vacancy associates facilitate photoexcitation of electrons and prevent the recombination of electron–hole pairs, which significantly enhances photocatalytic activity. This is demonstrated by the rapid mineralization of bisphenol A (10^{-5} M) with low photocatalyst loading (1 g L^{-1}), as well as enhanced bacterial disinfection. Improved electron–hole separation is also corroborated by enhanced photocatalytic reduction of nitrate.



INTRODUCTION

Many advanced processes of environmental significance, such as water or wastewater treatment and water splitting, are considering photocatalysis.^{1–5} One of the most important factors determining the efficiency and practical applicability of semiconductor photocatalysts is the ability to effectively generate photoinduced electron–hole (e–h) pairs and prevent their recombination.^{6–8} This has given rise to a growing interest in crystal engineering of photocatalytic materials, including morphological manipulation and doping of nanocrystals^{9–20} and control of exposed crystal facets.^{21–23}

Recent studies show that the type and abundance of atom vacancies in semiconductors strongly affect their photocatalytic activity.^{8,18} The electronic structures of semiconductors can significantly change at vacancy concentrations as low as one vacancy per one hundred million host atoms.²⁵ Vacancies in semiconductors can narrow the band gap, which facilitates both

Received: January 19, 2018

Revised: March 26, 2018

Accepted: May 3, 2018

Published: May 3, 2018

photoexcitation of electrons into the conduction band and e–h recombination.²⁶ However, for photocatalytic materials, the more important role of vacancies is to serve as adsorption sites and photoinduced charge carrier traps. Specifically, upon e–h separation, the charges can easily be transferred to the adsorbed species, which mitigates e–h recombination.^{27–29} Overall, the vacancy-induced enhanced e–h separation can significantly facilitate reactive oxygen species (ROS) generation and direct-hole oxidation of target pollutants.^{30,31} Improved e–h separation can also enhance photocatalytic reduction of oxidized priority pollutants by photogenerated electrons.^{32,33} Vacancy control is also a promising way to enhance other traits of semiconductors, such as electrocatalytic, magnetic, and thermoelectric properties.^{34,35}

Despite the significance of vacancies for efficient semiconductor photocatalysis, little is known about the mechanisms and engineering approaches that could be used to efficiently generate stable large vacancies. While vacancies can be generated from calcination of crystalline semiconductors, some intrinsic properties of nanocrystals (e.g., crystallinity and exposed facets) may be altered and their morphology can be damaged during heating.²⁶ Such unintended effects can be particularly undesirable for nanosheets, which often display higher catalytic efficiency. This underscores the need for improved understanding of mechanisms involved in the formation of vacancies. Recently, vacancy formation was shown to be closely related to the thickness of nanosheets: as the thickness of BiOCl nanosheets decreases to atomic scale, the predominant defects change from single Bi vacancy ($V_{\text{Bi}}^{\bullet\bullet}$) to triple vacancy associates ($V_{\text{Bi}}^{\bullet\bullet}V_{\text{O}}^{\bullet}V_{\text{Bi}}^{\bullet\bullet}$).²⁹ However, it is unknown whether other nanocrystals properties also significantly affect vacancy formation.

Here, we report a novel approach to induce vacancy formation on crystal surfaces to significantly enhance photocatalytic performance: the introduction of mesopores. We chose BiOCl as photocatalytic material because of its layered structure interleaved with $[\text{Bi}_2\text{O}_2]$ slabs and double halogen atoms slabs.³⁶ This structure not only minimizes recombination of e–h pairs due to its internal static electric fields but also facilitates characterization of vacancy types.³⁷ Positron annihilation analysis was used to characterize vacancy formation, and theoretical computations of the formation energy of isolated Bi vacancy were used to assess the significance of mesopores for the formation of large and stable vacancy associates. We also demonstrate that these unprecedentedly large vacancies enhance rapid and complete degradation of bisphenol A (BPA), bacterial disinfection, and NO_3^- reduction at relatively low photocatalyst loading. This new approach may advance the design of highly efficient photocatalysts.

■ EXPERIMENTAL SECTION

Synthesis of BiOCl-1, BiOCl-2, and Ultrathin BiOCl Nanosheets (UBN). We synthesized two hierarchical 3D BiOCl mesoporous nanostructures and compared their vacancy properties and photocatalytic activities. The two BiOCl nanostructures have similar morphology and exposed facets but are assembled from nanosheets of different thickness. All reagents were of analytical grade and used without further purification. To synthesize BiOCl-1, 3.0 mmol (1.46 g) of $\text{Bi}(\text{NO}_3)_3 \cdot 5\text{H}_2\text{O}$ and 0.0030 mmol (0.30 g) of polyethylene glycol 10000 (PEG10000) were dissolved in 30 mL of PEG400 by vigorously stirring for 10 min. Then, 3.0 mmol (0.175 g) of

NaCl was slowly added. After another 10 min of agitation, the mixture was sealed in a 50 mL Teflon-lined stainless-steel autoclave and heated at 180 °C for 24 h. Next, the mixture was gradually cooled to room temperature. A white precipitate was collected and washed with deionized water and absolute ethanol, and the product was kept in absolute ethanol for future use.

To synthesize BiOCl-2, 2.0 mmol (0.970 g) of $\text{Bi}(\text{NO}_3)_3 \cdot 5\text{H}_2\text{O}$ and 0.82 mmol (0.300 g) of cetrimonium bromide (CTAB) were dissolved in 25 mL of PEG400 by vigorously stirring for 10 min. Then, 2.0 mmol (0.117 g) of NaCl was slowly added. After another 10 min of agitation, the mixture was sealed in a 50 mL Teflon-lined stainless-steel autoclave and heated at 150 °C for 15 h. Next, the mixture was gradually cooled to room temperature. A white precipitate was collected and washed with deionized water and absolute ethanol, and the product was kept in absolute ethanol for future use.

The ultrathin BiOCl nanosheets (UBN) were synthesized using the method of Guan et al.²⁹ First, 1.0 mmol (0.486 g) of $\text{Bi}(\text{NO}_3)_3 \cdot 5\text{H}_2\text{O}$ was dissolved in 25 mL of 0.1 M mannitol solution by vigorously stirring for 10 min. Then, 5 mL of saturated NaCl solution was slowly added, yielding a uniform white suspension. After another 10 min of agitation, the mixture was transferred to a Teflon-lined stainless-steel autoclave of 45 mL capacity, heated at 160 °C for 3 h, and then cooled to room temperature. The resulting solid powder was collected by centrifugation and washed with deionized water repeatedly to remove residual ions. The final product was then dried at 60 °C for 4 h.

Material Characterization. The X-ray diffraction (XRD) spectra of the materials were recorded using an X-ray diffractometer (Rigaku D/max2500) with Cu K α radiation ($\lambda = 1.54056 \text{ \AA}$). The X-ray photoelectron spectroscopy (XPS) analysis was done using a Kratos Axis Ultra DLD XPS. The morphology of the BiOCl products was characterized with scanning electron microscopy (SEM) (Nova Nano SEM 230, FEI) and transmission electron microscopy (TEM) (Tecnai G² F20, FEI). The Brunauer–Emmett–Teller (BET) specific surface area of the products was analyzed by nitrogen adsorption using a Tristar 3000 nitrogen adsorption apparatus. The thickness of ultrathin BiOCl nanosheets was examined with atomic force microscopy (AFM) (Multimode8, Bruker).

The positron lifetime experiments were carried out using a fast–fast coincidence ORTEC system (Oak Ridge Technology & Engineering Cooperation) with a time resolution of ~ 240 ps in full width at half-maximum. A 30 μCi source of Na was sandwiched between two identical samples, and the total count was 1 million. Positron lifetime calculations were carried out using the ATSUP method,³⁸ in which the electron density and the positron crystalline Coulomb potential were constructed by the non-self-consistent superposition of free atom electron density and Coulomb potential in the absence of the positron. We used $3 \times 3 \times 2$ supercells for positron lifetime calculations of unrelaxed structure monovacancy defects and vacancy associates in BiOCl. To obtain the electron density and the Coulomb potential due to the nuclei and the electron density, several self-consistent calculations for electronic structures were performed with the fit-QMCGGA (QMC: quantum Monte Carlo; GGA: generalized gradient approximation) approach or electron–electron exchange correlations. To obtain the positron lifetimes, the GGA form of the enhancement factor proposed by Barbiellini et al. was chosen.³⁹

Photoelectrochemical properties were measured in a three-electrode configuration, which was composed of a counter electrode (Pt foil), a reference electrode (saturated calomel electrode (SCE)), and a working electrode (BiOCl electrode). The BiOCl electrodes were prepared using a spin-coating method. First, 50 mg of BiOCl-1 or BiOCl-2 was suspended in 2 mL of ethanol, and the mixture was ultrasonicated for 15 min to form a homogeneous suspension. Then, the suspension was spin-coated on a FTO substrate with a rate of 300 rpm for 20 s. This procedure was repeated 10 times. A 1 M sodium hydrate was used as the electrolyte. The current–time (i – t) curves were collected at 0 V vs SCE. A 300-W UV lamp was used as the light source.

Steady-state photoluminescence (PL) spectra were acquired on a luminescence spectrometer (Jobin Yvon Fluorolog 3-TAU). Transient absorption spectra (TAS) of charge carriers were obtained using the microsecond–millisecond (μ s–ms) time scale laser system. The sample preparation procedures were the same as those for photoelectrochemical measurements. A PTI GL-3300 nitrogen laser was used as the excitation source (380 nm, 0.4 mJ pulse^{−1}, 2 Hz, and 1 ns pulse duration), and a 100 W tungsten lamp provided the probe light. The signal was recorded with a digital oscilloscope (Tektronix TDS220) and transferred to a computer for analysis. All TAS signals were obtained following averaging of 100–300 pulses.

Electrochemical impedance spectroscopy (EIS) was measured at 0.0 V, using an impedance measurement unit of workstation in the frequency range of 0.1–10⁶ Hz with a sinusoidal ac perturbation of 5 mV. Approximately 0.1 g of as-prepared BiOCl powder was mixed with 1 mL of 2.5% PEG20000 solution and stirred for 30 min. A film was then made using the doctor-blade method on fluorine-doped tin oxide (FTO) conductive glass to obtain counter electrode (CE). EIS was executed on dummy cells with a typical symmetric sandwich-like structure (i.e., CE/electrolyte/CE).

Electron spin resonance (ESR) spectra (to characterize the photocatalytically generated ROS) were obtained using an ESR spectrometer (JEOL JES-FA200) at 300 K and 9.062 GHz.

Computational Details. The projector augmented wave (PAW) approach⁴⁰ was used in density functional theory (DFT) computations to represent the ion–electron interaction, as implemented in the Vienna ab initio simulation package (VASP).⁴¹ The electron exchange–correlation functional was treated using generalized gradient approximation (GGA) in the form proposed by Perdew, Burke and Ernzerhof (PBE).⁴² The energy precision was set to 10^{−5} eV, and atomic position was fully relaxed until the maximum force on each atom was less than 10^{−2} eV/Å. The 500 eV energy cut off was adopted, and Brillouin zone was sampled with a 11 × 11 × 1 Γ -centered Monkhorst–Pack k -points grid for geometry optimization and self-consistent calculations.

The BiOCl monolayer was cleaved from the bulk BiOCl crystal, which belongs to the tetragonal space group $P4/nmm$ (No. 129). The monolayers with and without pores were considered to compare the formation energies of a Bi vacancy within the monolayers. The isolated Bi vacancy was modeled by moving the appropriate-position Bi atoms from the monolayer, as schematically illustrated in Figure 3. The BiOCl monolayer sheet was placed in the xy plane with the z direction perpendicular to the layer plane, and a vacuum space of 16 Å in the z direction was used to avoid interactions between adjacent layers.

Photocatalytic Degradation Experiments. The photocatalytic activities of the BiOCl products were evaluated with the photocatalytic degradation experiments of aqueous bisphenol A (BPA), using an XPA-system photochemical reactor (Nanjing Xujiang Electromechanical Plant). Photocatalytic experiments were carried out under UV irradiation at room temperature. A 300 W Hg arc lamp was used as the light source to provide the UV light, and the light intensity was ~ 7 mW cm^{−2}. In a typical degradation experiment, 0.11 mmol (0.050 g) of a BiOCl material was dispersed in 50 mL of BPA aqueous solution (1×10^{-5} M). Prior to light irradiation, the suspension was stirred for 1 h in the dark to reach adsorption equilibrium of BPA on the photocatalyst. Then, the reaction was initiated, and 4 mL of the suspension was withdrawn every hour and centrifuged to remove the catalyst. The concentration of BPA was analyzed using UV–vis spectroscopy (characteristic absorption peak of BPA at $\lambda = 275$ nm). The intermediates from the photocatalytic oxidation of BPA were monitored using high-performance liquid chromatography (HPLC)/mass spectrometry (MS) (Waters Xevo TQ-S) with full scan from m/z 100 to 300 in positive electrospray ionization mode.

Photocatalytic Reduction Experiments. The equipment used to test the photocatalytic reduction of NO₃[−] was the same as that used in BPA oxidation experiments. In a typical reduction experiment, 0.11 mmol (0.050 g) of BiOCl and 0.05 mmol (0.004 g) of sodium acetate were dispersed in 50 mL of NO₃[−] solution (NaNO₃ was used as NO₃[−] source and the initial NO₃[−] concentration was 6.77 mg-N L^{−1}). Prior to initiating the reduction experiment, argon was bubbled into the aqueous suspension through a diffuser for 30 min to remove dissolved oxygen. Samples (4 mL) were withdrawn every 20 min and centrifuged to remove the catalyst, and the filtrate was analyzed to determine NO₃[−], NO₂[−], and NH₄⁺ concentrations by ion chromatography (IC, Dionex ICS5000). N₂ was also analyzed, using a gas chromatograph (GC, Agilent 7890A-5973) equipped with a thermal conductivity detector, to calculate the total nitrogen balance.

Bacterial Disinfection Assays. Overnight cultured *E. coli* (DH5a) was suspended in phosphate buffer saline (PBS) to a final concentration of about 10⁶ cells mL^{−1}. BiOCl-1 or BiOCl-2 (200 mg mL^{−1}) was then added into the suspensions, and the suspensions were irradiated with an ultraviolet analyzer (6 mW cm^{−2}, $\lambda = 365$ nm, ZF-5, Kanghua, China) for the indicated durations. The cells were then stained by propidium iodide (PI, final concentration of 1 μ g mL^{−1}) for 5 min and observed by fluorescence microscopy (BX51, Olympus, USA). At least 10 fields were examined. The PI-positive (dead) cells and the total cells were counted, and the percentage of PI-positive cells was calculated for different treatments.

All experiments were carried out in triplicates. Differences between groups were examined using Student's t test ($p < 0.05$). Statistical analyses were conducted using Statistical Packages for the Social Sciences (SPSS) Version 20.0.

RESULTS AND DISCUSSION

Two Mesoporous Nanostructures Assembled from BiOCl Nanosheets of Different Thicknesses Exhibited Similar Morphology and Exposed Facets but Different Vacancies. TEM images of BiOCl-1 and BiOCl-2 show that the flower-like architectures are composed of nanosheets (Figure 1a,b), with BiOCl-1 having much thinner nanosheets (3–6 nm) than BiOCl-2 (10–20 nm) (Figures 1c,d and S4). XRD patterns (Figure S1) and XPS analysis (Figure S2)

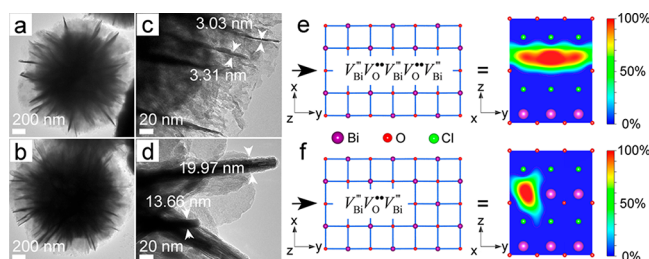


Figure 1. Transmission electron microscopy (TEM) images showing that two nanosheet-assembled 3D nanostructures BiOCl-1 and BiOCl-2 have similar morphology, but the nanosheets of BiOCl-1 are thinner than those of BiOCl-2. TEM images of BiOCl-1 (a) and BiOCl-2 (b) corroborate the presence of flower-like architectures with similar morphology and size. The thickness of nanosheets in BiOCl-1 is 3–6 nm (c), and the thickness of nanosheets in BiOCl-2 is 10–20 nm (d). Schematic representations of trapped positrons of $V_{\text{Bi}}^{\text{III}}V_{\text{O}}^{\text{II}}V_{\text{Bi}}^{\text{III}}V_{\text{O}}^{\text{II}}V_{\text{Bi}}^{\text{III}}$ (e) and $V_{\text{Bi}}^{\text{III}}V_{\text{O}}^{\text{II}}V_{\text{Bi}}^{\text{III}}$ (f) vacancy associates based on positron annihilation data.

Table 1. Positron Lifetime Parameters of BiOCl-1 and BiOCl-2^a

nanostructures	τ_1 (ps)	τ_2 (ps)	τ_3 (ns)	I_1 (%)	I_2 (%)	I_3 (%)
BiOCl-1	268	393	3.57	55.1	44.7	0.149
BiOCl-2	260	363	2.98	53.1	46.7	0.156

^a τ : positron lifetime components of different types of defects. I : relative intensity of different types of defects.

Table 2. Theoretically Calculated Positron Lifetime (τ) Values of Different Types of Defects in BiOCl^a

defect type	bulk	$V_{\text{Bi}}^{\text{III}}$	$V_{\text{Bi}}^{\text{III}}V_{\text{O}}^{\text{II}}$	$V_{\text{Bi}}^{\text{III}}V_{\text{O}}^{\text{II}}V_{\text{Bi}}^{\text{III}}$	$V_{\text{Bi}}^{\text{III}}V_{\text{O}}^{\text{II}}V_{\text{Bi}}^{\text{III}}V_{\text{O}}^{\text{II}}V_{\text{Bi}}^{\text{III}}$
τ (ps)	215	242	248	260	276

^a τ : positron lifetime components of different types of defects.

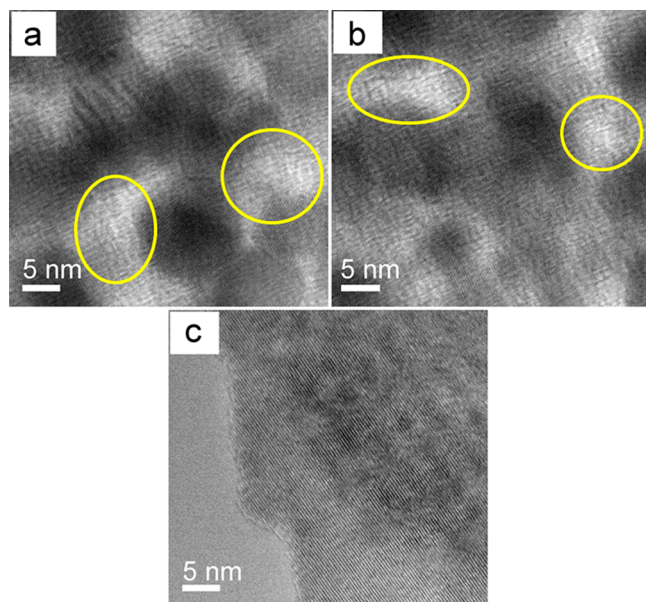


Figure 2. High resolution transmission electron microscopy (HR-TEM) images showing that mesopores are present on the nanosheets of BiOCl-1 (a) and BiOCl-2 (b) but not on the ultrathin BiOCl nanosheets (UBN) (c). The yellow circles indicate the pores.

indicate that both BiOCl nanostructures are pure tetragonal BiOCl, and SEM images (Figure S3) corroborate that BiOCl-1

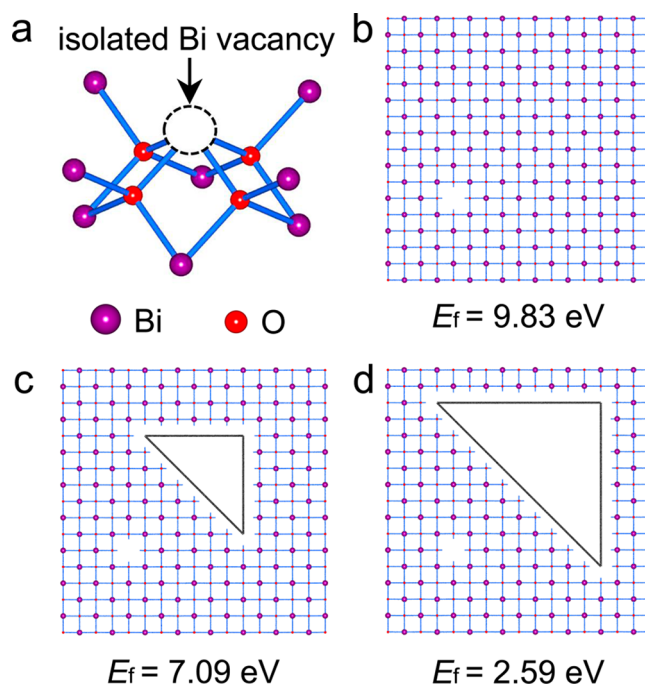


Figure 3. Computational results demonstrating formation of Bi vacancy is energetically more favorable for nanosheets containing mesopores. Plot (a) shows the coordination environment of isolated Bi vacancy. The E_f values represent formation energy of Bi atom vacancy in different types of BiOCl nanosheets, including a 9 nm² nanosheet without pores (b), a 9 nm² nanosheet with a 0.83 nm² pore (c), and a 9 nm² nanosheet with a 2.86 nm² pore (d). A smaller E_f value indicates a higher likelihood of Bi vacancy formation.

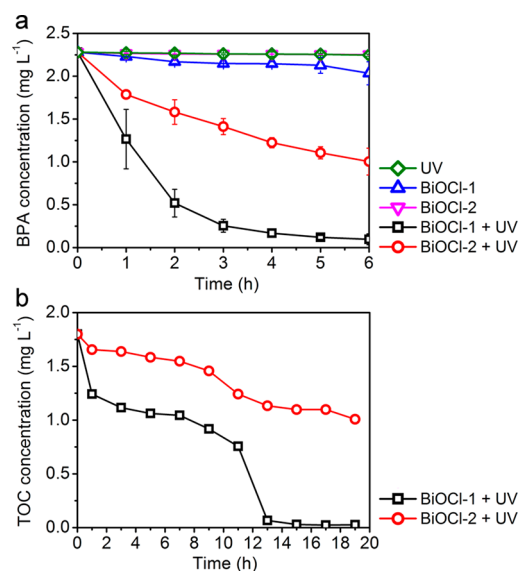


Figure 4. Photodegradation of bisphenol A (BPA) showing higher photocatalytic activity of BiOCl-1 than BiOCl-2. Panel (a) shows photodegradation of BPA under UV irradiation ($\sim 7 \text{ mW cm}^{-2}$, $\lambda = 365 \text{ nm}$) in the presence of different BiOCl nanostructures (1 g L^{-1}); the initial concentration of BPA was 2.28 mg L^{-1} (10^{-5} M). Error bars represent \pm one standard deviation from the mean ($n = 3$). Panel (b) shows mineralization kinetics of BPA as indicated by the decrease of total organic carbon (TOC) in the presence of different BiOCl nanostructures (1 g L^{-1}); the initial TOC concentration was 1.8 mg L^{-1} .

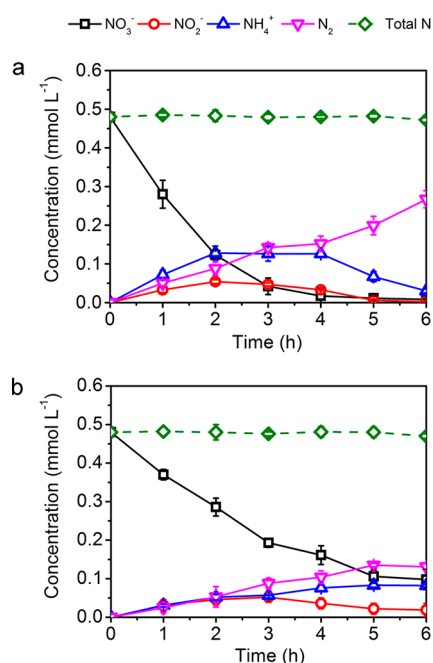


Figure 5. Photoreduction of NO_3^- was more effective with BiOCl-1 (with larger vacancies) than with BiOCl-2. Experiments were conducted with 1 g L^{-1} of BiOCl-1 (a) or BiOCl-2 (b), both irradiated by UV light ($\sim 7 \text{ mW cm}^{-2}$, $\lambda = 365 \text{ nm}$). No reduction of NO_3^- was observed in the absence of BiOCl (i.e., UV irradiation alone) or without UV irradiation (Figure S18). Error bars represent \pm one standard deviation from the mean ($n = 3$).

and BiOCl-2 both consist entirely of uniform flower-like architectures. High resolution TEM (HR-TEM) analysis confirm the highly crystalline nature of the two BiOCl nanostructures (Figure S5a,b), and the corresponding selected-area electron diffraction (SAED) patterns reveal that both BiOCl nanostructures have the (001) facet as the dominant exposed facets (Figure S5c,d). Both BiOCl-1 and BiOCl-2 are mesoporous materials; the average pore sizes are 11.9 nm for BiOCl-1 and 12.1 nm for BiOCl-2 (Figure S6). The BET surface areas of BiOCl-1 and BiOCl-2 are 42.1 and $31.9 \text{ m}^2 \text{ g}^{-1}$, respectively.

We monitored the vacancies of the two BiOCl nanostructures using positron annihilation (Figure S7). As an accurate method to characterize defects in solids, positron annihilation spectrometry can provide information on the type and relative concentration of defects/vacancies by measuring the lifetime of positrons, even at the parts-per-million level.^{43,44} Both BiOCl-1 and BiOCl-2 yielded three lifetime components, τ_1 , τ_2 , and τ_3 (Table 1), based on experimental lifetime of positrons. The lifetime component τ_1 is generally attributed to the Bi–O vacancy associates, whereas the components with longer lifetimes (τ_2 and τ_3) are assigned to the large defect clusters and the interface present in a material, respectively.²⁸ Larger-sized defects/vacancies lead to lower average electron density, thus reducing the annihilation rate and increasing the positron lifetime.⁴⁵ Thus, a larger τ value would indicate the presence of larger defects/vacancies. The measured τ_1 for BiOCl-2 is 260 ps , corresponding to the $V_{\text{Bi}}^{\text{III}}V_{\text{O}}^{\text{II}}V_{\text{Bi}}^{\text{III}}$ vacancy associates, based on the theoretically calculated positron lifetime values of different types of vacancies of BiOCl using the atomic superposition (ATSUP) method (Table 2). In contrast, the experimentally measured τ_1 value of BiOCl-1 (268 ps) indicates that BiOCl-1

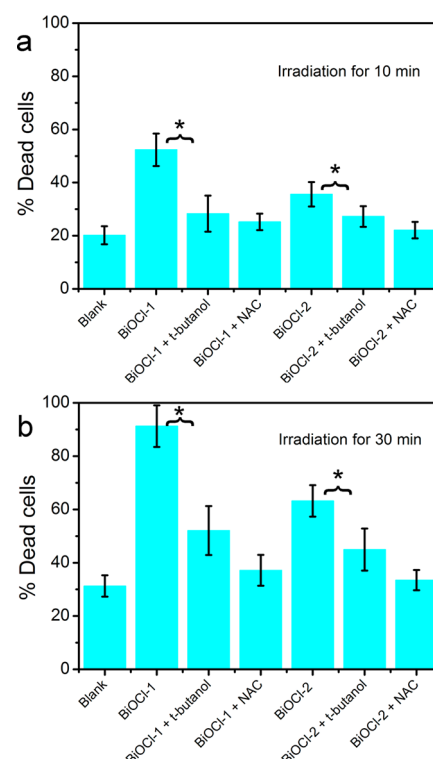


Figure 6. Disinfection of *E. coli* DH5a ($10^6 \text{ cells mL}^{-1}$) in phosphate buffer saline (PBS) was more effective with BiOCl-1 (with larger vacancies) than with BiOCl-2 (each at 200 mg mL^{-1}) under (a) 10 min and (b) 30 min of exposure to UV (6 mW cm^{-2} , $\lambda = 365 \text{ nm}$). N-Acetyl-L-cysteine (NAC, 1 mmol L^{-1}) was used as a scavenger for all ROS species, and *t*-butanol (1 mmol L^{-1}) as $\cdot\text{OH}$ scavenger. The asterisks “*” indicate a significant difference between the groups ($p < 0.05$). Error bars represent \pm one standard deviation from the mean ($n = 3$).

possessed larger vacancies than BiOCl-2. Specifically, besides $V_{\text{Bi}}^{\text{III}}V_{\text{O}}^{\text{II}}V_{\text{Bi}}^{\text{III}}$ vacancy associates, $V_{\text{Bi}}^{\text{III}}V_{\text{O}}^{\text{II}}V_{\text{Bi}}^{\text{III}}V_{\text{O}}^{\text{II}}V_{\text{Bi}}^{\text{III}}$ vacancy associates were also present on the crystal surfaces of BiOCl-1. The schematic illustrations of $V_{\text{Bi}}^{\text{III}}V_{\text{O}}^{\text{II}}V_{\text{Bi}}^{\text{III}}$ and $V_{\text{Bi}}^{\text{III}}V_{\text{O}}^{\text{II}}V_{\text{Bi}}^{\text{III}}V_{\text{O}}^{\text{II}}V_{\text{Bi}}^{\text{III}}$ vacancy associates on BiOCl are depicted on the basis of the theoretical calculation of the two types of Bi–O vacancy associates (Figure 1e,f). The relative intensity (I) of the positron lifetime provides information on the concentration of the vacancies. For both BiOCl-1 and BiOCl-2, the relative intensity of τ_1 accounts for over 50% of the total defects, indicating that Bi–O vacancy associates are the predominant forms of defects.^{46,47}

Nanosheet Thickness Alone Cannot Explain the Formation of Large-Sized Vacancies on BiOCl Nanostructures. When the thickness of BiOCl nanosheets decreases to atomic scale, the predominant vacancies on BiOCl crystal surface change from single $V_{\text{Bi}}^{\text{III}}$ to larger $V_{\text{Bi}}^{\text{III}}V_{\text{O}}^{\text{II}}V_{\text{Bi}}^{\text{III}}$ vacancy associates.²⁹ Thus, a potential explanation for the existence of larger vacancies associates (i.e., $V_{\text{Bi}}^{\text{III}}V_{\text{O}}^{\text{II}}V_{\text{Bi}}^{\text{III}}V_{\text{O}}^{\text{II}}V_{\text{Bi}}^{\text{III}}$) on BiOCl-1 than on BiOCl-2 might be that BiOCl-1 is assembled from thinner nanosheets. However, the difference in nanosheet thickness alone cannot explain this result. The nanosheet thickness of BiOCl-1, for which large amounts of $V_{\text{Bi}}^{\text{III}}V_{\text{O}}^{\text{II}}V_{\text{Bi}}^{\text{III}}V_{\text{O}}^{\text{II}}V_{\text{Bi}}^{\text{III}}$ were detected, is 3 to 6 nm . If nanosheet thickness were the only factor controlling the formation of large vacancies, we should not have observed such large vacancies on BiOCl-1, since they were not detected on the thinner 2.7 nm

BiOCl nanosheets (for which only $V_{\text{Bi}}^{\text{III}}V_{\text{O}}^{\bullet\bullet}V_{\text{Bi}}^{\text{III}}$ vacancy associates were detected).²⁹ To the best of our knowledge, the extraordinarily large $V_{\text{Bi}}^{\text{III}}V_{\text{O}}^{\bullet\bullet}V_{\text{Bi}}^{\text{III}}V_{\text{O}}^{\bullet\bullet}V_{\text{Bi}}^{\text{III}}$ vacancy associates have never been reported before. Apparently, other factor(s) besides nanosheet thickness influenced the formation of the unique large surface vacancies.

Presence of Mesopores Is Vital for the Formation of Quintuple Vacancy Associates. To understand the potential role of nanosheet surface morphology in the formation of large vacancies, we examined the surface features of BiOCl-1 and BiOCl-2, as well as a 2.7 nm-thick ultrathin BiOCl nanosheet product (referred to as “UBN” hereafter) synthesized according to the literature²⁹ (detailed characterization data of UBN are shown in Table S1 and Figures S8–S11). A distinct difference between UBN and the nanosheets of the two BiOCl nanostructures is that the surfaces of the latter had much larger pores. As indicated by the HR-TEM images (Figure 2),^{48,49} significant amounts of mesopores were observed on the nanosheets of both BiOCl-1 and BiOCl-2 but not on UBN. The pores on the two BiOCl nanostructures were likely formed during the Ostwald ripening process during crystal formation, because the nanosheets of the BiOCl products were assembled from BiOCl nanoparticles. To understand the correlation between the presence of pores and the existence of vacancies, we calculated the formation energies, E_f , of Bi atom vacancy in different types of BiOCl nanosheets, including a 9 nm² nanosheet without pores, a 9 nm² nanosheet with a 0.83 nm² pore, and a 9 nm² nanosheet with a 2.86 nm² pore (Figure 3). A smaller E_f value indicates that the formation of Bi vacancy is energetically more favorable, resulting in a higher likelihood of finding Bi vacancies on BiOCl nanosheets. The formation energy of the Bi vacancy can be defined as⁵⁰

$$E_f = E_{\text{Bi-vacancy}} + \mu_{\text{Bi}} - E_{\text{original}}$$

where E_{original} is the total energy of the BiOCl monolayer without Bi vacancy; $E_{\text{Bi-vacancy}}$ is the total energy of the BiOCl monolayer with an isolated Bi vacancy; μ_{Bi} is the energy of one Bi atom taking into account the spin effect (1.32 eV). The calculated E_f values are 9.83 eV for the nanosheet without pores, 7.09 eV for the one with a 0.83 nm² pore, and 2.59 eV for the one with a 2.86 nm² pore. The order of E_f values indicates that Bi vacancies on BiOCl nanosheets should be energetically more favorable for nanosheets with pores, which is consistent with the experimentally determined vacancy properties of the three products.

On the basis of these computational results, we propose the following conceptual model to explain how mesopores induce the formation of large vacancies. Along the perimeters of the mesopores, there are many incompletely coordinated Bi and O atoms. These atoms tend to bond with each other, which stretches the bonds between the incompletely coordinated atoms and those immediately adjacent. Accordingly, the formation of vacancies near the mesopores counterbalances the thermodynamic instability of the system caused by the stretching of the bonds. Overall, the presence of mesopores can lower the formation energy of vacancies.

Larger-Sized Vacancies Resulted in Enhanced Photocatalytic Activity. Large vacancies are known to facilitate photoexcitation of electrons and prevent the recombination of e–h pairs, resulting in enhanced photocatalytic ROS generation and direct-hole oxidation of target contaminants.^{24,30} We compared the photoelectrical responses of BiOCl-1 and BiOCl-2 (Figure S12). The photocurrent density of BiOCl-1

reached 0.14 mA cm^{−2} under UV irradiation, approximately 7 times that of BiOCl-2. Therefore, BiOCl-1 had greater photoexcitation capability, which was corroborated by steady-state PL measurements showing a lower PL quantum yield of BiOCl-1 than that of BiOCl-2 (Figure S13a). Such drastic PL quenching was likely due to the greater charge carrier extraction efficiency for BiOCl-1.⁵¹ In addition, the dynamics of photogenerated charge carrier can be directly monitored with TAS, on the basis of the characteristic bleaching profile of the semiconductors.⁵² Note that the photogenerated electrons in BiOCl-1 displayed a longer lifetime than those of BiOCl-2 (the time for the concentration of charge carriers to decrease by half of its initial value, $t_{50\%}$, was 1182 ns for BiOCl-1 versus 861 ns for BiOCl-2; Figure S13b), which demonstrates that large vacancies effectively mitigate the recombination of e–h pairs.

EIS analysis also indicates higher photocatalytic activity of BiOCl-1 than BiOCl-2.^{53,54} Figure S14 shows the Nyquist plots of BiOCl-1 and BiOCl-2 under UV irradiation. Two semicircles in EIS were observed for each of the two BiOCl products. The diameter of the arc in the middle-frequency region represents the charge-transfer resistance, which is the most important factor affecting catalytic activity.⁵⁵ Evidently, the diameter of the arc of BiOCl-1 is smaller than that of BiOCl-2, corroborating the greater catalytic activity of BiOCl-1 and further confirming the significant effects of vacancies on the changes of electronic structures of the materials.

To verify the effects of large vacancies on photocatalytic activities, we compared the photocatalytic oxidation activities of BiOCl-1 and BiOCl-2 under UV irradiation (~ 7 mW cm^{−2}, $\lambda = 365$ nm), using BPA as the model target compound. BPA is a relatively recalcitrant endocrine disruptor that is commonly detected in water.⁵⁶ Figure 4a shows that no measurable degradation of BPA occurred in the absence of the BiOCl photocatalysts nor in the presence of the BiOCl but without UV irradiation. UV-irradiated BiOCl-1 (1.0 g L^{−1}) removed 96% BPA after 6 h, versus only 55% BPA removal with BiOCl-2. More importantly, the total organic carbon (TOC) data show that photocatalytic treatment with BiOCl-1 resulted in near complete (96%) mineralization of BPA upon 13 h of UV irradiation, compared to only 35% for BiOCl-2 (Figure 4b). Such high degree of mineralization of organic carbon by BiOCl-based photocatalysts is unprecedented.

We also compared the ROS production activity of BiOCl-1 versus BiOCl-2 under UV irradiation, using 5,5-dimethyl-1-pyrroline *N*-oxide (DMPO) spin-trapped electron spin resonance (ESR) spectroscopy. Both $\cdot\text{OH}$ and $\text{O}_2^{\bullet-}$ were generated by BiOCl-1 and BiOCl-2 (Figure S15). Radical-trapping experiments were carried out to clarify the roles of different ROS in the photocatalytic degradation process (Figure S16). In the presence of *t*-butanol (a $\cdot\text{OH}$ scavenger), BPA removal over 3 h with BiOCl-1 decreased by 56%, compared to only 17% with BiOCl-2. This reflects the importance of hydroxyl radicals for treatment with BiOCl-1, which is consistent with the more effective e–h separation by BiOCl-1 that results in enhanced hole generation and associated formation of water-derived $\cdot\text{OH}$. In contrast, when superoxide dismutase was used to trap $\text{O}_2^{\bullet-}$, BPA degradation after 6 h with BiOCl-1 was reduced by only 24%, compared to 33% with BiOCl-2. Moreover, when ammonium oxalate was used as a scavenger of holes, BPA degradation with BiOCl-1 or BiOCl-2 was inhibited to similar extents (42% and 45%, respectively). Thus, ROS scavenging experiments indicate that the higher

catalytic efficiency of BiOCl-1 is due to its higher $\cdot\text{OH}$ generation capacity.

Differences in the predominant types of ROS produced may lead to different degradation pathways. Therefore, the intermediates formed during BPA photocatalytic degradation were analyzed. In both experiments with BiOCl-1 and BiOCl-2, the product ion at m/z (number of protons/number of charges) 227 was detected and identified as the deprotonated molecule $[(M - H)]$ of BPA. When BiOCl-1 was used as the photocatalyst, a total of three product ions (m/z 135, 133, 121) were identified. The concentrations of the three intermediates increased initially and then decreased gradually (Figure S17a). In contrast, when BiOCl-2 was the photocatalyst, only two product ions (m/z 133, 121) were identified. More importantly, the intermediates were not further degraded within the tested time frame, as their concentrations leveled off after approximately 19 h. The patterns shown in Figure S17 are consistent with the results of TOC removal (Figure 4b) and clearly show that BiOCl-1 was more effective in degrading BPA into small organic acids and eventually into inorganic molecules (e.g., CO_2 and water).

To further verify the greater photocatalytic efficiency of BiOCl-1, we compared the BPA degradation capabilities of the two BiOCl materials under conditions relevant to wastewater tertiary treatment. These experiments were carried out with BPA in diluted secondary effluent (Table S2). BiOCl-1 outperformed BiOCl-2 achieving 2.5-fold higher BPA removal (37% vs 14%) upon 6 h of UV irradiation (Figure S18).

We also compared the ability of BiOCl-1 versus BiOCl-2 to photocatalytically reduce nitrate, which is a common target during wastewater treatment to prevent eutrophication⁵⁷ and is a frequent cause of drinking water standards violations, especially in rural areas.⁵⁸ Consistent with its higher $e-h$ separation efficiency, BiOCl-1 exhibited higher NO_3^- removal efficiency than BiOCl-2 (98.3% vs 79.5%) as well as a higher extent of reduction (e.g., 56.6% vs 34.7% conversion to N_2) upon 6 h of UV irradiation ($\sim 7 \text{ mW cm}^{-2}$, $\lambda = 365 \text{ nm}$) (Figures 5 and S19). The higher reduction capacity of BiOCl-1 is consistent with the larger yield and longer lifetimes of its photogenerated electrons (Figure S13).

BiOCl-1 was also more effective for bacterial disinfection, killing 91% of *E. coli* (DH5a) cells ($10^6 \text{ cells mL}^{-1}$) upon UV irradiation for 30 min (compared to 66% for irradiated BiOCl-2 and 31% for UV alone) (Figure 6). The greater bactericidal effects of BiOCl-1 is also attributable to its higher efficiency for generating $\cdot\text{OH}$, which led to more severe damage to the bacterial cells. Furthermore, the photocatalytic activity of UBN (tested with BPA degradation, nitrate reduction, and bacterial disinfection) was higher than that of BiOCl-2 but lower than that of BiOCl-1 (Figure S20), which is consistent with the differences in vacancy type among these three materials.

Overall, the formation of large vacancy associates (as demonstrated with our model BiOCl nanosheets) holds great promise for enhancing the efficiency and practical applicability of both oxidative and reductive photocatalytic water treatment. This can be accomplished by surmounting thermodynamic instability through the introduction of mesopores, which represents a practical innovation to lower the formation energy of large vacancies on crystalline nanosheets. Benchmarking with commercially available photocatalysts would be needed to assess the practical use of BiOCl-based photocatalysts. Nevertheless, this novel insight on generating stable large vacancies advances fundamental understanding of nanomaterial

structure–activity relationships and underscores significant opportunities for enhancing semiconductor photocatalysis through nanocrystal engineering.

■ ASSOCIATED CONTENT

Supporting Information

The Supporting Information is available free of charge on the ACS Publications website at DOI: 10.1021/acs.est.8b00352.

XRD patterns, XPS spectra, SEM/TEM images, N_2 adsorption/desorption isotherms, positron annihilation spectra, atomic force microscopy image, transient photocurrent density test, PL spectra and transient absorption spectroscopy, EIS spectra, radical-trapping experiments, mineralization kinetics and reaction pathways, and photodegradation BPA activity of two BiOCl nanostructures in wastewater treatment plant effluent (PDF)

■ AUTHOR INFORMATION

Corresponding Authors

*E-mail: chenwei@nankai.edu.cn (W.C.).

*E-mail: liul@nankai.edu.cn (L.L.).

*E-mail: alvarez@rice.edu (P.J.J.A.).

ORCID

Hai-jun Zhang: 0000-0002-9082-3662

Wei Chen: 0000-0003-2106-4284

Lu Liu: 0000-0002-0143-0198

Pedro J. J. Alvarez: 0000-0002-6725-7199

Notes

The authors declare no competing financial interest.

■ ACKNOWLEDGMENTS

This work was supported by the National Natural Science Foundation of China (Grants 21425729, 21271108, 21403001, and 21701125), Tianjin Municipal Science and Technology Commission (Grant 11JCZDJC24800), China Postdoctoral Science Foundation (2015M580208), 111 Program of Ministry of Education of China (T2017002), Fundamental Research Funds for the Central Universities, and the NSF ERC on Nanotechnology-Enabled Water Treatment (EEC-1449500).

■ REFERENCES

- (1) Hoffmann, M. R.; Martin, S. T.; Choi, W.; Bahnemann, D. W. Environmental Applications of Semiconductor Photocatalysis. *Chem. Rev.* **1995**, *95*, 69–96.
- (2) Long, M. C.; Brame, J.; Qin, F.; Bao, J. M.; Li, Q. L.; Alvarez, P. Phosphate Changes Effect of Humic Acids on TiO_2 Photocatalysis: From Inhibition to Mitigation of Electron-Hole Recombination. *Environ. Sci. Technol.* **2017**, *51*, 514–521.
- (3) Dhakshinamoorthy, A.; Asiri, A. M.; García, H. Metal-Organic Framework (MOF) Compounds: Photocatalysts for Redox Reactions and Solar Fuel Production. *Angew. Chem., Int. Ed.* **2016**, *55*, 5414–5445.
- (4) Park, H.; Choi, W.; Hoffmann, M. R. Effects of the Preparation Method of the Ternary $\text{CdS/TiO}_2/\text{Pt}$ Hybrid Photocatalysts on Visible Light-Induced Hydrogen Production. *J. Mater. Chem.* **2008**, *18*, 2379–2385.
- (5) Choi, H.; Kim, Y. J.; Varma, R. S.; Dionysiou, D. D. Thermally Stable Nanocrystalline TiO_2 Photocatalysts Synthesized via Sol-Gel Methods Modified with Ionic Liquid and Surfactant Molecules. *Chem. Mater.* **2006**, *18*, 5377–5384.
- (6) Xiao, X.; Zhu, W. W.; Liu, Q. Y.; Yuan, H.; Li, W. W.; Wu, L. J.; Li, Q.; Yu, H. Q. Impairment of Biofilm Formation by TiO_2

Photocatalysis through Quorum Quenching. *Environ. Sci. Technol.* **2016**, *50*, 11895–11902.

(7) Anand, S.; Thekkepat, K.; Waghmare, U. V. Two-Dimensional Rectangular and Honeycomb Lattices of NbN: Emergence of Piezoelectric and Photocatalytic Properties at Nanoscale. *Nano Lett.* **2016**, *16*, 126–131.

(8) Li, H.; Shang, J.; Zhu, H. J.; Yang, Z. P.; Ai, Z. H.; Zhang, L. Z. Oxygen Vacancy Structure Associated Photocatalytic Water Oxidation of BiOCl. *ACS Catal.* **2016**, *6*, 8276–8285.

(9) Qu, Y. Q.; Liao, L.; Cheng, R.; Wang, Y.; Lin, Y. C.; Huang, Y.; Duan, X. F. Rational Design and Synthesis of Freestanding Photoelectric Nanodevices as Highly Efficient Photocatalysts. *Nano Lett.* **2010**, *10*, 1941–1949.

(10) Hernández-Alonso, M. D.; Fresno, F.; Suárez, S.; Coronado, J. Development of Alternative Photocatalysis to TiO₂: Challenges and Opportunities. *Energy Environ. Sci.* **2009**, *2*, 1231–1257.

(11) Duan, H. H.; Yan, N.; Yu, R.; Chang, C. R.; Zhou, G.; Hu, H. S.; Rong, H. P.; Niu, Z. Q.; Mao, J. J.; Asakura, H.; Tanaka, T.; Dyson, P.; Li, J.; Li, Y. D. Ultrathin Rhodium Nanosheets. *Nat. Commun.* **2014**, *5*, 3093–3100.

(12) Wang, J. F.; Zhong, Y.; Wang, L.; Zhang, N.; Cao, R. H.; Bian, K. F.; Alarid, L.; Haddad, R.; Bai, F.; Fan, H. Y. Morphology-Controlled Synthesis and Metalation of Porphyrin Nanoparticles with Enhanced Photocatalytic Performance. *Nano Lett.* **2016**, *16*, 6523–6528.

(13) Kim, H. I.; Weon, S.; Kang, H.; Hagstrom, A. L.; Kwon, O. S.; Lee, Y. S.; Choi, W.; Kim, J. H. Plasmon-Enhanced Sub-Bandgap Photocatalysis via Triplet-Triplet Annihilation Upconversion for Volatile Organic Compound Degradation. *Environ. Sci. Technol.* **2016**, *50*, 11184–11192.

(14) Muñoz-Batista, M. J.; Gómez-Cerezo, M. N.; Kubacka, A.; Tudela, D.; Fernández-García, M. Role of Interface Contact in CeO₂-TiO₂ Photocatalytic Composite Materials. *ACS Catal.* **2014**, *4*, 63–72.

(15) Zhou, W.; Li, W.; Wang, J. Q.; Qu, Y.; Yang, Y.; Xie, Y.; Zhang, K. F.; Wang, L.; Fu, H. G.; Zhao, D. Y. Ordered Mesoporous Black TiO₂ as Highly Efficient Hydrogen Evolution Photocatalyst. *J. Am. Chem. Soc.* **2014**, *136*, 9280–9283.

(16) Fujito, H.; Kunioku, H.; Kato, D.; Suzuki, H.; Higashi, M.; Kageyama, H.; Abe, R. Layered Perovskite Oxychloride Bi₄Nb₈O₈Cl: A Stable Visible Light Responsive Photocatalyst for Water Splitting. *J. Am. Chem. Soc.* **2016**, *138*, 2082–2085.

(17) Pan, C. S.; Takata, T.; Nakabayashi, M.; Matsumoto, T.; Shibata, N.; Ikuhara, Y.; Domen, K. A Complex Perovskite-Type Oxynitride: The First Photocatalyst for Water Splitting Operable at up to 600 nm. *Angew. Chem., Int. Ed.* **2015**, *54*, 2955–2959.

(18) Manna, G.; Bose, R.; Pradhan, N. Photocatalytic Au-Bi₂S₃ Heteronanostructures. *Angew. Chem., Int. Ed.* **2014**, *53*, 6743–6746.

(19) Choi, J.; Park, H.; Hoffmann, M. R. Effects of Single Metal-Ion Doping on the Visible-Light Photoreactivity of TiO₂. *J. Phys. Chem. C* **2010**, *114*, 783–792.

(20) Jassby, D.; Budarz, J. F.; Wiesner, M. Impact of Aggregate Size and Structure on the Photocatalytic Properties of TiO₂ and ZnO Nanoparticles. *Environ. Sci. Technol.* **2012**, *46*, 6934–6941.

(21) Pathakoti, K.; Morrow, S.; Han, C.; Pelaez, M.; He, X. J.; Dionysiou, D. D.; Hwang, H. M. Photoinactivation of *Escherichia coli* by Sulfur-Doped and Nitrogen-Fluorine-Codoped TiO₂ Nanoparticles under Solar Simulated Light and Visible Light Irradiation. *Environ. Sci. Technol.* **2013**, *47*, 9988–9996.

(22) Bi, Y. P.; Ouyang, S. X.; Umezawa, N.; Cao, J. Y.; Ye, J. H. Facet Effect of Single-Crystalline Ag₃PO₄ Sub-microcrystals on Photocatalytic Properties. *J. Am. Chem. Soc.* **2011**, *133*, 6490–6492.

(23) Jiang, J.; Zhao, K.; Xiao, X. Y.; Zhang, L. Z. Synthesis and Facet-Dependent Photoreactivity of BiOCl Single-Crystalline Nanosheets. *J. Am. Chem. Soc.* **2012**, *134*, 4473–4476.

(24) Lei, F. C.; Sun, Y. F.; Liu, K. T.; Gao, S.; Liang, L.; Pan, B. C.; Xie, Y. Oxygen Vacancies Confined in Ultrathin Indium Oxide Porous Sheets for Promoted Visible-Light Water Splitting. *J. Am. Chem. Soc.* **2014**, *136*, 6826–6829.

(25) Wang, H.; Zhang, J. J.; Hang, X. D.; Zhang, X. D.; Xie, J. F.; Pan, B. C.; Xie, Y. Half-Metallicity in Single-Layered Manganese Dioxide Nanosheets by Defect Engineering. *Angew. Chem., Int. Ed.* **2015**, *54*, 1195–1199.

(26) Kong, M.; Li, Y. Z.; Chen, X.; Tian, T. T.; Fang, P. F.; Zheng, F.; Zhao, X. J. Tuning the Relative Concentration Ratio of Bulk Defects to Surface Defects in TiO₂ Nanocrystals Leads to High Photocatalytic Efficiency. *J. Am. Chem. Soc.* **2011**, *133*, 16414–16417.

(27) Li, H.; Shang, J.; Yang, Z. P.; Shen, W. J.; Ai, Z. H.; Zhang, L. Z. Oxygen Vacancy Associated Surface Fenton Chemistry: Surface Structure Dependent Hydroxyl Radicals Generation and Substrate Dependent Reactivity. *Environ. Sci. Technol.* **2017**, *51*, 5685–5694.

(28) Liu, X. W.; Zhou, K. B.; Wang, L.; Wang, B. Y.; Li, Y. D. Oxygen Vacancy Clusters Promoting Reducibility and Activity of Ceria Nanorods. *J. Am. Chem. Soc.* **2009**, *131*, 3140–3141.

(29) Guan, M. L.; Xiao, C.; Zhang, J.; Fan, S. J.; An, R.; Cheng, Q. M.; Xie, J. F.; Zhou, M.; Ye, B. J.; Xie, Y. Vacancy Associates Promoting Solar-Driven Photocatalytic Activity of Ultrathin Bismuth Oxychloride Nanosheets. *J. Am. Chem. Soc.* **2013**, *135*, 10411–10417.

(30) Li, H.; Shang, J.; Ai, Z. H.; Zhang, L. Z. Efficient Visible Light Nitrogen Fixation with BiOBr Nanosheets of Oxygen Vacancies on the Exposed {001} Facets. *J. Am. Chem. Soc.* **2015**, *137*, 6393–6399.

(31) Naldoni, A.; Allietta, M.; Santangelo, S.; Marelli, M.; Fabbri, F.; Cappelli, S.; Bianchi, C. L.; Psaro, R.; Santo, V. D. Effect of Nature and Location of Defects on Bandgap Narrowing in Black TiO₂ Nanoparticles. *J. Am. Chem. Soc.* **2012**, *134*, 7600–7603.

(32) Nakajima, T.; Tamaki, Y.; Ueno, K.; Kato, E.; Nishikawa, T.; Ohkubo, K.; Yamazaki, Y.; Morimoto, T.; Ishitani, O. Photocatalytic Reduction of Low Concentration of CO₂. *J. Am. Chem. Soc.* **2016**, *138*, 13818–13821.

(33) Hirayama, J.; Kamiya, Y. Combining the Photocatalyst Pt/TiO₂ and the Nonphotocatalyst SnPd/Al₂O₃ for Effective Photocatalytic Purification of Groundwater Polluted with Nitrate. *ACS Catal.* **2014**, *4*, 2207–2215.

(34) Laraoui, A.; Hodges, J. S.; Meriles, C. A. Nitrogen-Vacancy-Assisted Magnetometry of Paramagnetic Centers in an Individual Diamond Nanocrystal. *Nano Lett.* **2012**, *12*, 3477–3482.

(35) Bai, S.; Ge, J.; Wang, L. L.; Gong, M.; Deng, M. S.; Kong, Q.; Song, L.; Jiang, J.; Zhang, Q.; Luo, Y.; Xie, Y.; Xiong, Y. J. A Unique Semiconductor-Metal-Graphene Stack Design to Harness Charge Flow for Photocatalysis. *Adv. Mater.* **2014**, *26*, 5689–5695.

(36) Zhao, K.; Zhang, L. Z.; Wang, J. J.; Li, Q. X.; He, W. W.; Yin, J. J. Surface Structure-Dependent Molecular Oxygen Activation of BiOCl Single-Crystalline Nanosheets. *J. Am. Chem. Soc.* **2013**, *135*, 15750–15753.

(37) Zhao, S.; Zhang, Y. W.; Zhou, Y. M.; Zhang, C.; Sheng, X. L.; Fang, J. S.; Zhang, M. Y. Reactable Polyelectrolyte-Assisted Synthesis of BiOCl with Enhanced Photocatalytic Activity. *ACS Sustainable Chem. Eng.* **2017**, *5*, 1416–1424.

(38) Puska, M. J.; Nieminen, R. M. Theory of Positrons in Solids and on Solid Surfaces. *Rev. Mod. Phys.* **1994**, *66*, 841–897.

(39) Barbiellini, B.; Puska, M. J.; Korhonen, T.; Harju, A.; Torsti, T.; Nieminen, R. M. Calculation of Positron States and Annihilation in Solids: A Density-Gradient-Correction Scheme. *Phys. Rev. B: Condens. Matter Mater. Phys.* **1996**, *53*, 16201–16213.

(40) Kresse, G.; Joubert, D. From Ultrasoft Pseudopotentials to the Projector Augmented-Wave Method. *Phys. Rev. B: Condens. Matter Mater. Phys.* **1999**, *59*, 1758–1775.

(41) Kresse, G.; Hafner, J. *Ab Initio* Molecular-Dynamics Simulation of the Liquid-Metal-Amorphous-Semiconductor Transition in Germanium. *Phys. Rev. B: Condens. Matter Mater. Phys.* **1994**, *49*, 14251–14265.

(42) Perdew, J. P.; Wang, Y. Accurate and Simple Analytic Representation of the Electron-Gas Correlation Energy. *Phys. Rev. B: Condens. Matter Mater. Phys.* **1992**, *45*, 13244–13249.

(43) Wu, Y. H.; Yuan, B.; Li, M. R.; Zhang, W. H.; Liu, Y.; Li, C. Well-Defined BiOCl Colloidal Ultrathin Nanosheets: Synthesis, Characterization, and Application in Photocatalytic Aerobic Oxidation of Secondary Amines. *Chem. Sci.* **2015**, *6*, 1873–1878.

- (44) Feng, F.; Guo, H. Y.; Li, D. Q.; Wu, C. Z.; Wu, J. C.; Zhang, W. S.; Fan, S. J.; Yang, Y. C.; Wu, X. J.; Yang, J. L.; Ye, B. J.; Xie, Y. Highly Efficient Photothermal Effect by Atomic-Thickness Confinement in Two-Dimensional ZrNCl Nanosheets. *ACS Nano* **2015**, *9*, 1683–1691.
- (45) Lyu, M. J.; Liu, Y. W.; Zhi, Y. D.; Xiao, C.; Gu, B. C.; Hua, X. M.; Fan, S. J.; Lin, Y.; Bai, W.; Tong, W.; Zou, Y. M.; Pan, B. C.; Ye, B. J.; Xie, Y. Electric-Field-Driven Dual Vacancies Evolution in Ultrathin Nanosheets Realizing Reversible Semiconductor to Half-Metal Transition. *J. Am. Chem. Soc.* **2015**, *137*, 15043–15048.
- (46) Li, Z.; Xiao, C.; Fan, S. J.; Deng, Y.; Zhang, W. S.; Ye, B. J.; Xie, Y. Dual Vacancies: An Effective Strategy Realizing Synergistic Optimization of Thermoelectric Property in BiCuSeO. *J. Am. Chem. Soc.* **2015**, *137*, 6587–6593.
- (47) Jiao, X. C.; Chen, Z. W.; Li, X. D.; Sun, Y. F.; Gao, S.; Yan, W. S.; Wang, C. M.; Zhang, Q.; Lin, Y.; Luo, Y.; Xie, Y. DefectMediated Electron-Hole Separation in One-Uni-Cell ZnIn_2S_4 Layers for Boosted Solar-Driven CO_2 Reduction. *J. Am. Chem. Soc.* **2017**, *139*, 7586–7594.
- (48) Phillip, W. A.; Dorin, R. M.; Werner, J.; Hoek, E. M. V.; Wiesner, U.; Elimelech, M. Tuning Structure and Properties of Graded Triblock Terpolymer-Based Mesoporous and Hybrid Films. *Nano Lett.* **2011**, *11*, 2892–2900.
- (49) Carter, R.; Oakes, L.; Douglas, A.; Muralidharan, N.; Cohn, A. P.; Pint, C. L. A Sugar-Derived Room-Temperature Sodium Sulfur Battery with Long Term cycling Stability. *Nano Lett.* **2017**, *17*, 1863–1869.
- (50) Chai, G. L.; Lin, C. S.; Wang, J. Y.; Zhang, M. Y.; Wei, J.; Cheng, W. D. Density Functional Theory Simulations of Structures and Properties for Ag-Doped ZnO Nanotubes. *J. Phys. Chem. C* **2011**, *115*, 2907–2913.
- (51) Zhu, Z. L.; Ma, J. N.; Wang, Z. L.; Mu, C.; Fan, Z. T.; Du, L. L.; Bai, Y.; Fan, L. Z.; Yan, H.; Phillips, D. L.; Yang, S. H. Efficiency Enhancement of Perovskite Solar Cells Through Fast Electron Extraction: The Role of Graphene Quantum Dots. *J. Am. Chem. Soc.* **2014**, *136*, 3760–3763.
- (52) Jing, L. Q.; Cao, Y.; Cui, H. Q.; Durrant, J. R.; Tang, J. W.; Liu, D. N.; Fu, H. G. Acceleration Effects of Phosphate Modification on the Decay Dynamics of Photo-Generated Electrons of TiO_2 and Its Photocatalytic Activity. *Chem. Commun.* **2012**, *48*, 10775–10777.
- (53) Pan, M. L.; Zhang, Y. Y.; Shan, C.; Zhang, X. L.; Gao, G. D.; Pan, B. C. Flat Graphene-Enhanced Electron Transfer Involved in Redox Reactions. *Environ. Sci. Technol.* **2017**, *51*, 8597–8605.
- (54) Guo, S. Q.; Wang, L. C.; Zhang, C. G.; Qi, G. C.; Gu, B. C.; Liu, L.; Yuan, Z. H. A Unique Semiconductor–Carbon–Metal Hybrid Structure Design as a Counter Electrode in Dye-Sensitized Solar Cells. *Nanoscale* **2017**, *9*, 6837–6845.
- (55) Wei, W. Q.; Liu, D.; Wei, Z.; Zhu, Y. F. Short-Range π - π Stacking Assembly on P25 TiO_2 Nanoparticles for Enhanced Visible-Light Photocatalysis. *ACS Catal.* **2017**, *7*, 652–663.
- (56) Torres, R. A.; Pétrier, C.; Combet, E.; Moulet, F.; Pulgarin, C. Bisphenol A Mineralization by Integrated Ultrasound-UV-Iron (III) Treatment. *Environ. Sci. Technol.* **2007**, *41*, 297–302.
- (57) Kim, D. H.; Lee, J.; Ryu, J.; Kim, K.; Choi, W. Arsenite Oxidation Initiated by the UV Photolysis of Nitrite and Nitrate. *Environ. Sci. Technol.* **2014**, *48*, 4030–4037.
- (58) Pennino, M. J.; Compton, J. E.; Leibowitz, S. G. Trends in Drinking Water Nitrate Violations Across the United States. *Environ. Sci. Technol.* **2017**, *51*, 13450–13460.